ACSNANO

www.acsnano.org

ARTICLE

Compound Meta-Optics for Complete and Loss-Less Field Control

Hanyu Zheng, Mingze He, You Zhou, Ivan I. Kravchenko, Joshua D. Caldwell, and Jason G. Valentine*

Cite This: *ACS Nano* 2022, 16, 15100−15107

Read Online

ABSTRACT: Optical metasurfaces offer a compact platform for manipulation of the amplitude, phase, and polarization state of light. Independent control over these properties, however, is hindered by the symmetric transmission matrix associated with single-layer metasurfaces. Here, we utilize multilayer birefringent meta-optics to realize high-efficiency, independent control over the amplitude, phase, and polarization state of light. High-efficiency control is enabled by redistributing the wavefront between cascaded metasurfaces, while end-to-end inverse design is used to realize independent complex-valued functions for orthogonal polarization states. Based on this platform, we demonstrate spatial mode division multiplexing, optical mode conversion, and universal vectorial holograms, all with diffraction efficiencies over 80%. This meta-optic platform expands the design space of flat optics and could lead to advances in optical communications, quantum entanglement, and information encryption.

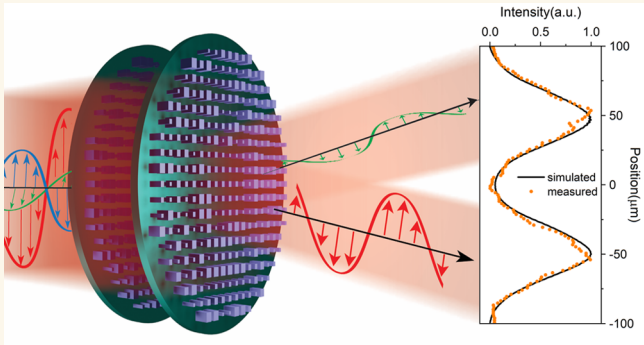

KEYWORDS: *compound meta-optics, inverse design, spatial division multiplexing, mode conversion, vectorial holography*

The ability to independently control the amplitude, phase, and polarization state of light is needed for a wide variety of scientific and industrial applications and generally requires multiple conventional optical elements such as lenses, polarizers, and amplitude masks. The need for multiple elements results in large systems that can be difficult to integrate into compact optical packages. Optical metasurfaces, comprising subwavelength scale meta-atoms, provide a versatile platform for manipulating optical waves in a compact form factor[1−4] and have been used to create a wide variety of optical elements such as lenses,[5−7] beam splitters,[8−11] and waveplates.[12,13] Metasurfaces, moreover, can go beyond the simple replacement of conventional optics by providing extraordinary functionalities including multifunctional imaging,[14−16] phase-mining,[17] image processing,[18,19] augment reality,[20,21] holography,[22−25] and vectorial field manipulation.[26−28]

Although metasurface-based wavefront control has been demonstrated in the past,[29−32] independent control of phase and amplitude using a single metasurface comes at the expense of a polarization-dependent response, as illustrated in Figure 1a. The involvement of polarizer components introduces loss that can be as high as 90% in some circumstances.[33] Moreover, the symmetric Jones matrix that dictates the transmission of each meta-atom prevents independent control over polarization conversion for orthogonal axes.[26] Spatial multiplexing

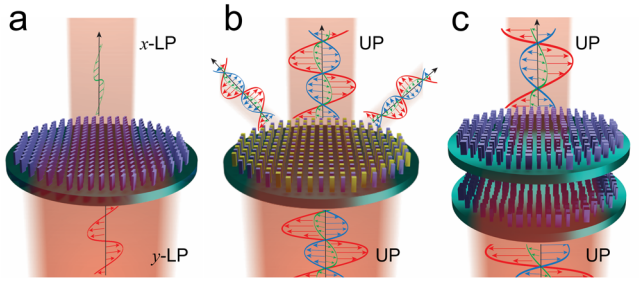

Figure 1. Complex-field control with metasurfaces. (a) Single metasurface, in the absence of a supercell, enables full and independent control (phase, amplitude, polarization) over one input polarization state. LP stands for linear polarized. (b) Use of supercells enables interference to be used for independent control over unpolarized light but results in loss to higher diffraction orders. UP stands for unpolarized. (c) Bilayer meta-optics can be used for near loss-less full field control for unpolarized light.

Received: June 24, 2022
Accepted: August 22, 2022
Published: August 26, 2022

https://doi.org/10.1021/acsnano.2c06248
ACS Nano 2022, 16, 15100−15107

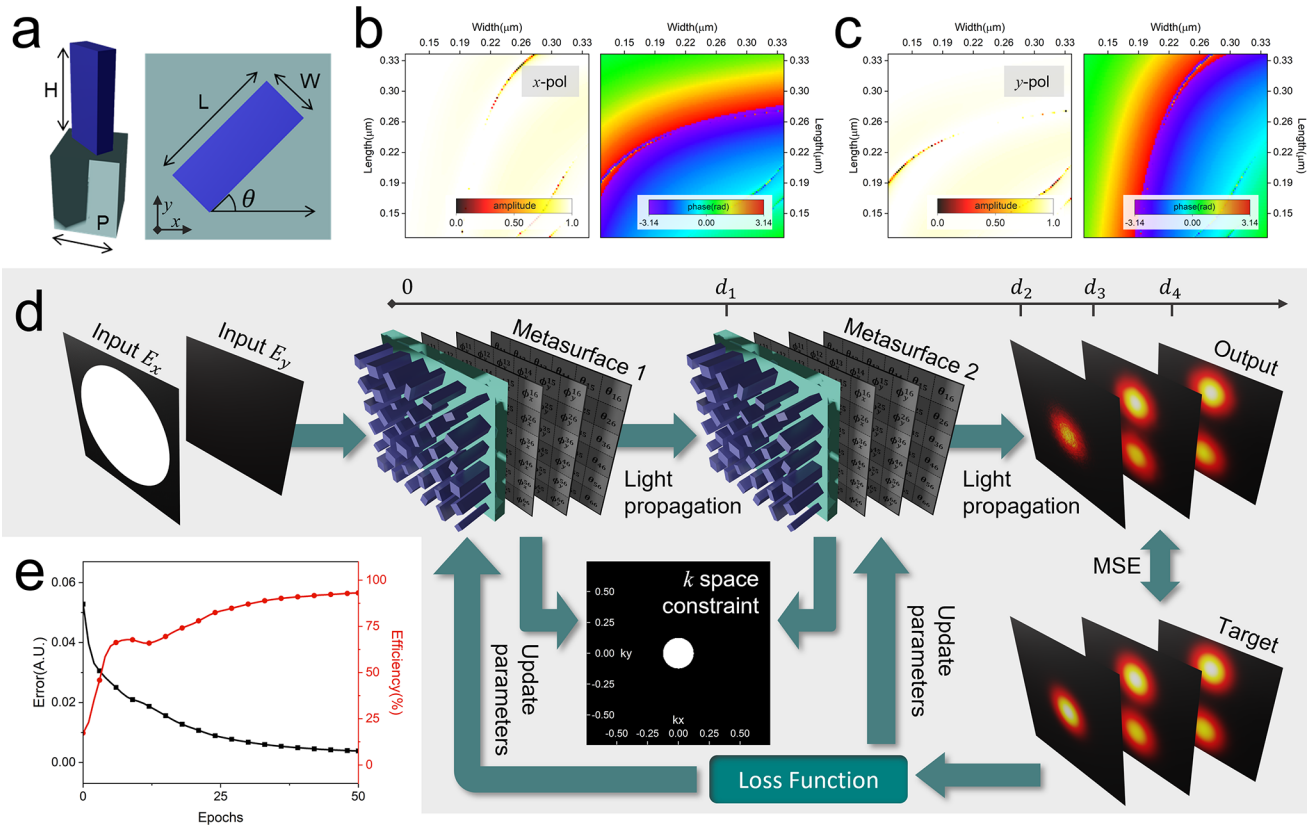

Figure 2. Inverse design of multilayer meta-optics. (a) Schematic of the birefringent meta-atom. (b and c) Transmission coefficient (amplitude and phase) map of the meta-atom under x and y polarized illumination, respectively, as a function of the geometry (width and length). In these maps, the rotation angle of the meta-atom was fixed at 0°. (d) Inverse design architecture allows for optimization of the amplitude, phase, and polarization state. Multiple optimization targets with various propagation distances, indicated by the coordinate (d_2, d_3, d_4), were sampled for robustness. (e) Error function and efficiency of the meta-optic as a function of epoch.

can provide independent polarization manipulation over orthogonal states by using interference between the neighboring meta-atoms, as shown in Figure 1b. This method, however, leads to higher diffraction orders[32] due to the use of a larger supercell, limiting the diffraction efficiency in the target order. An alternative approach is the use of multilayer, compound meta-optics that harness independent design degrees of freedom in each layer[34−36] and allow for light redistribution during propagation for realizing near loss-less amplitude and phase functions.[37,38]

In this work, we expand on the multilayer meta-optic platform[38−42] to perform complex-amplitude manipulation for orthogonal polarization states by employing end-to-end design optimization. In this platform, shown in Figure 1c, birefringent meta-atoms are used for both surfaces, enabling independent control over orthogonal polarization states as well as polarization conversion between those states. Redistribution of the wavefront between metasurface layers allows for nearly loss-less, complex-valued wavefront and polarization control, which is not limited by the symmetric Jones matrix (a more detailed discussion can be found in S1 of the Supporting Information). As a proof of concept, we experimentally demonstrate a meta-optic for optical mode manipulation,[43−46] including a spatial division multiplexer (SDM), an optical mode converter, and a vectorial hologram. All the devices achieve experimental diffraction efficiencies above 80%, showing excellent agreement with the theoretical prediction.

RESULTS AND DISCUSSION

The experimentally demonstrated meta-optic consists of two metasurfaces with near-unity transmission, each serving to control the phase delay and polarization conversion between the x- and y-directions. In the design process, we utilized meta-atoms comprising α-silicon nanopillars with a height of 0.75 μm and a period of 0.52 μm, sitting on a silica substrate, as shown in Figure 2a. The design wavelength was 1.15 μm, and the polarization-dependent transmission coefficient map was calculated using rigorous coupled wave analysis (RCWA). The width and length of the nanopillars varied between 0.12 and 0.34 μm and the transmission and phase maps are presented in Figure 2b,c, demonstrating near-unity transmission and independent control over phase along the x- and y-axes. This data forms the data library that is used in the design process of the compound meta-optics.

In order to achieve full control over phase, amplitude, and the polarization state of light, the incident field is divided into two separate channels, E_x and E_y, with each comprising a complex-amplitude field matrix. Based on the data library, each metasurface can independently control the phase along the x- and y-directions, as well as the polarization conversion, which is determined by the rotation angle, θ, of the meta-atom. The transmitted field of each rectangular nanopillar comprising the metasurface follows an analytical model based on the Jones matrix given by,

https://doi.org/10.1021/acsnano.2c06248
ACS Nano 2022, 16, 15100−15107

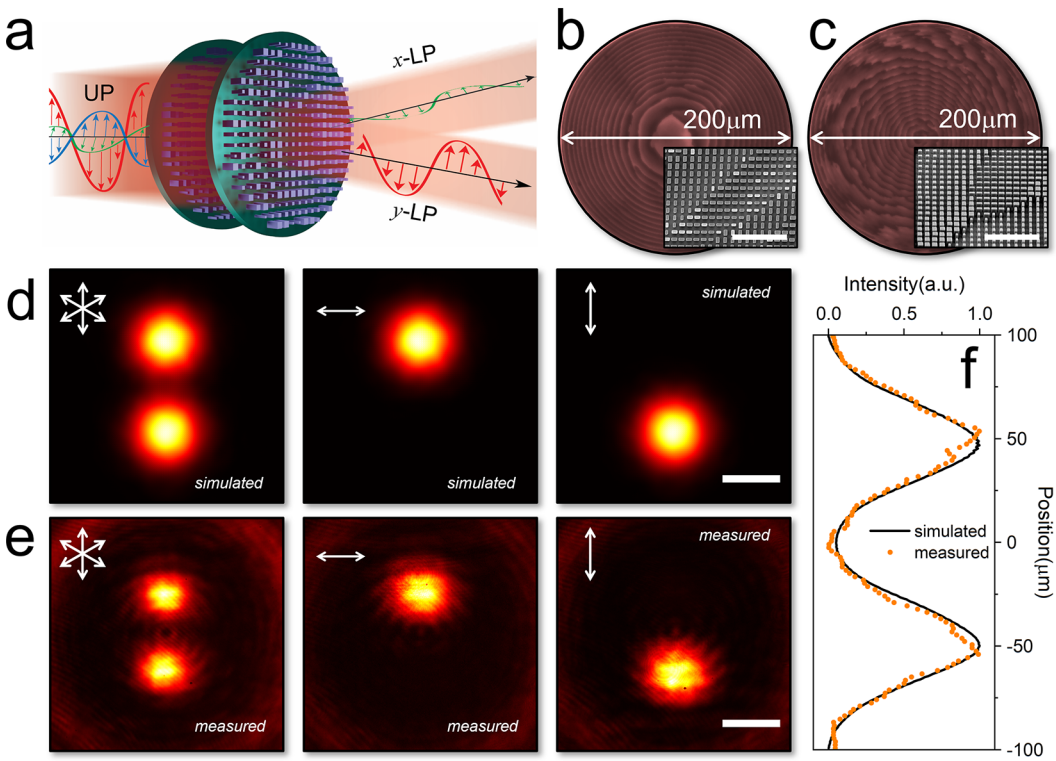

Figure 3. Meta-optic-based SDM to unpolarized light. (a) Schematic of the multilayer meta-optic for SDM to unpolarized beams. (b and c) Optical images of each metasurface in the meta-optic. The insets are SEM images of metasurfaces. Scale bar: 4 μm. (d and e) Simulated and measured polarization-dependent intensity distributions after the meta-optic. An unpolarized supercontinuum laser was used as the source. The arrows in the upper-left corner indicate the analyzer direction, which are unpolarized (left), *x*-polarized (middle), and *y*-polarized (right). Scale bar: 50 μm. (f) Simulated and measured mode profile after the meta-optic as a function of lateral position. The intensity has been normalized to the maximum value.

$$\begin{bmatrix} E_{x,\mathrm{out}} \\ E_{y,\mathrm{out}} \end{bmatrix} = \begin{bmatrix} \cos(\theta) & \sin(\theta) \\ -\sin(\theta) & \cos(\theta) \end{bmatrix} \begin{bmatrix} e^{i\phi_x} & 0 \\ 0 & e^{i\phi_y} \end{bmatrix} \begin{bmatrix} \cos(\theta) & -\sin(\theta) \\ \sin(\theta) & \cos(\theta) \end{bmatrix} \begin{bmatrix} E_{x,\mathrm{in}} \\ E_{y,\mathrm{in}} \end{bmatrix} = \mathcal{M}(\phi_x, \phi_y, \theta) \begin{bmatrix} E_{x,in} \\ E_{y,in} \end{bmatrix} \tag{1}$$

where $E_{x,\,\mathrm{in}}$, $E_{y,\,\mathrm{in}}$ and $E_{x,\,\mathrm{out}}$, $E_{y,\,\mathrm{out}}$ are the x and y polarized incident and transmitted amplitude, respectively. ϕ_x and ϕ_y are the phase shifts provided by the resonator for x and y polarization, values that are dictated by the size of the resonator. θ is the pillar rotation angle, which determines the polarization conversion efficiency and transmitted phase for a given meta-atom in the metasurface. M represents the operator of Jones matrix.

To design the multilayer meta-optic, we employed an end-to-end inverse-design algorithm, as shown in Figure 2d, which is based on a physical model of light propagation within the meta-system. In previous work,[38] we designed loss-less meta-optic phase profiles based on the Gerchberg-Saxton (GS) algorithm, which did not allow for the design of the polarization state and required *a priori* knowledge of the desired intensity distribution at the second metasurface layer. In this work, we utilize a stochastic gradient descent (SGD) solver,[47] a common approach in machine learning applications, to specify the output intensity, phase, and polarization at a position in space after the last metasurface in the optic. In the forward analytical model, light propagating in free space is described by the angular spectrum propagation operator,

$$\mathcal{R}(d) = \mathcal{F}^{-1}\mathcal{H}(d)\mathcal{F} \tag{2}$$

where F is a Fourier transform operator, d is the propagating distance, and $\mathcal{H}(d) = \exp[i\cdot(2\pi d/\lambda)\cdot\sqrt{1 - k_x^{\,2} - k_y^{\,2}}]$ is the transfer function of light in k-space. Here, λ is the effective wavelength in the medium and k_x and k_y represent the lateral wavenumbers. Light propagating through the meta-optic is calculated by cascading the various elements and free-space regions and is given by,

$$E(x, y, p_{\mathrm{out}}) = \mathcal{R}(d_2)\mathcal{M}(\phi_{x2}, \phi_{y2}, \theta_2)\mathcal{R}(d_1)\mathcal{M}(\phi_{x1}, \phi_{y1}, \theta_1)E(x, y, p_{\mathrm{in}}) \tag{3}$$

where p is the polarization state. Equation 3 provides the optical response of a bilayer meta-optic and analytically connects the input electric fields $E_{x,\,\mathrm{in}}$ and $E_{y,\,\mathrm{in}}$ with the output fields,$E_{x,\,\mathrm{out}}$ and $E_{y,\,\mathrm{out}}$. This approach can be readily extended for many-layer systems, such as diffractive neural networks,[48] going beyond the more traditional GS algorithm-based optimization.

To avoid overfitting in the training process, multiple output fields at various propagation distances were optimized simultaneously. Due to the complex-valued electric fields, the error function, defined by the mean square error (MSE), was calculated using both the real and imaginary components of the output field as well as the polarization states at each propagation distance. The target field profiles used to design the compound meta-optics in this manuscript are presented in the Supporting Information (S2). The error gradient of the designable parameters was then calculated by the SGD solver,

https://doi.org/10.1021/acsnano.2c06248
ACS Nano 2022, 16, 15100−15107

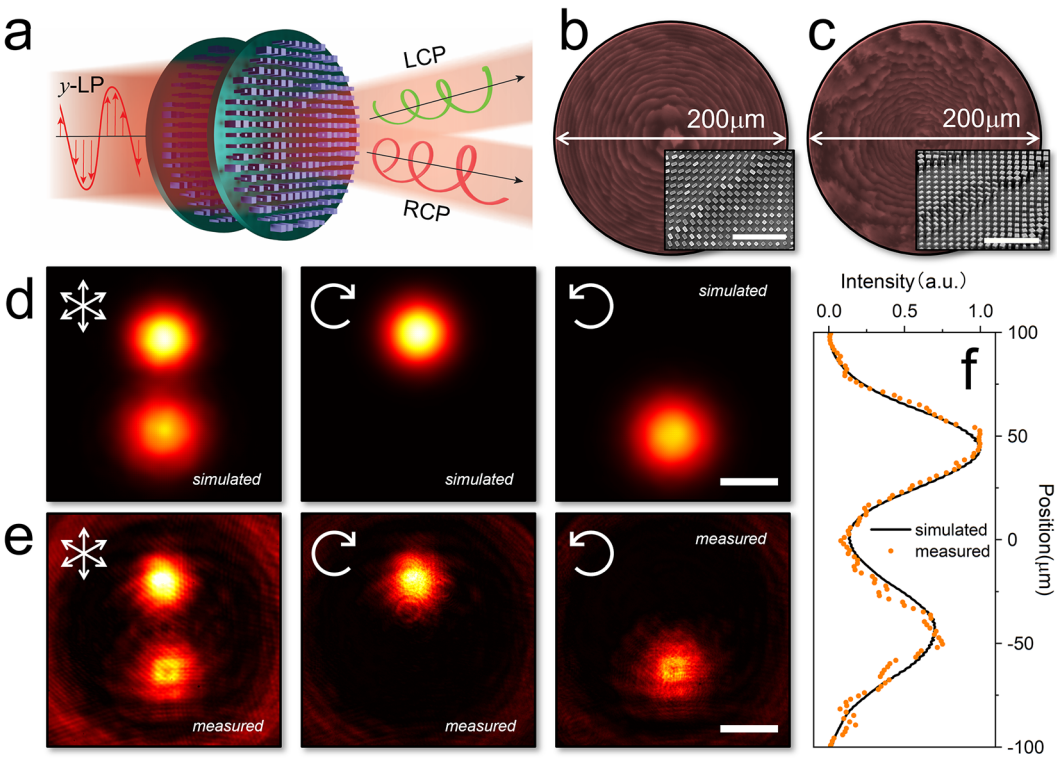

Figure 4. Meta-optic-based mode conversion for circularly polarized light. (a) Schematic of the multilayer meta-optic for mode conversion to linearly polarized beams. (b and c) Optical images of each metasurface in the meta-optic. The insets are SEM images of metasurfaces. Scale bar: 4 μm. (d and e) Simulated and measured polarization-dependent intensity distributions after the meta-optic. An unpolarized supercontinuum laser was used as the source. The upper-left corner arrows indicate the analyzer orientation, which are unpolarized (left), LCP (middle), and RCP (right). Scale bar: 50 μm. (f) Simulated and measured mode profile after the meta-optic as a function of lateral position. The intensity has been normalized to the maximum value.

which was used to update all parameters simultaneously. The evolution of the error function, as well as the absolute efficiency, defined by the energy in the target mode over the input power, is presented in Figure 2e. Near-unity efficiency is achieved in roughly 50 training cycles (epochs). In addition, an angular filter was employed at the output field from each metasurface as a constraint during optimization iterations as shown in Figure 2d. There are two main purposes for this restriction. First, a k-space filter will remove light propagating at high angles between the metasurfaces, mitigating the dependence of the optical response on the angle of incidence. Second, the angular spectrum filter will reduce the required phase gradient of each metasurface resulting in more gradual meta-atom changes and reduced scattering. Ultimately, the k-space filter results in higher efficiency meta-optics, and a comparison of the optimized phase profile with/without the angular spectrum filter is presented in the Supporting Information (S3).

To experimentally validate the design methodology, each optimized metasurface was realized by starting with a wafer comprising a 0.75 μm thick silicon device layer on quartz. The silicon device layer was patterned into nanopillars with a period of 0.52 μm using electron beam lithography (EBL) followed by reactive ion etching (RIE). A PMMA layer was spin-coated over each metasurface as a protective coating as well as serving as an index-matching layer. The two metasurfaces were aligned using a custom alignment and bonding system (see details in the Supporting Information (S4)) with PDMS being used as the bonding material. Alignment of the metasurfaces was aided by fabricating an alignment mark consisting of a metasurface hologram, designed to project an alignment symbol at the prescribed separation distance. Final alignment was accomplished by observing the output intensity distribution of the meta-optic while tunning the lateral position of the metasurfaces (see fabrication details in the Methods section).

As a proof of concept, we optimized a series of bilayer meta-optics with an aperture size of 200 μm. The separation distance between layers was set at 287.5 μm, which was chosen to balance the spatial resolution of the designed amplitude function and the sensitivity to the angle of incidence.[49] We first designed and fabricated a meta-optic that operates as both a mode sorter and mode shaper for free-space spatial division multiplexing (SDM),[43] as shown in Figure 3a. The meta-optic splits incident light into x- and y-polarization states while, at the same time, transforming the two wavefronts into Gaussian profiles. Specifically, the desired output field at the second metasurface is given by a superposition of two Gaussian beams with the same beam waist,

$$\begin{bmatrix} E_x \\ E_y \end{bmatrix} = \begin{bmatrix} e^{-(r/28.3\lambda_0)^2} e^{ik_0 y \cdot \sin(0.03^\circ)} \\ e^{-(r/28.3\lambda_0)^2} e^{ik_0 y \cdot \sin(-0.03^\circ)} \end{bmatrix} \tag{4}$$

where λ_0 is designed working wavelength, k_0 is the free-space wavenumber, and r is the radial distance from the center of the aperture. In this case, since the proposed function is polarization independent, the rotation angle, θ, was fixed at 0° for all metasurface pixels. The optimized phase profile for

https://doi.org/10.1021/acsnano.2c06248
ACS Nano 2022, 16, 15100−15107

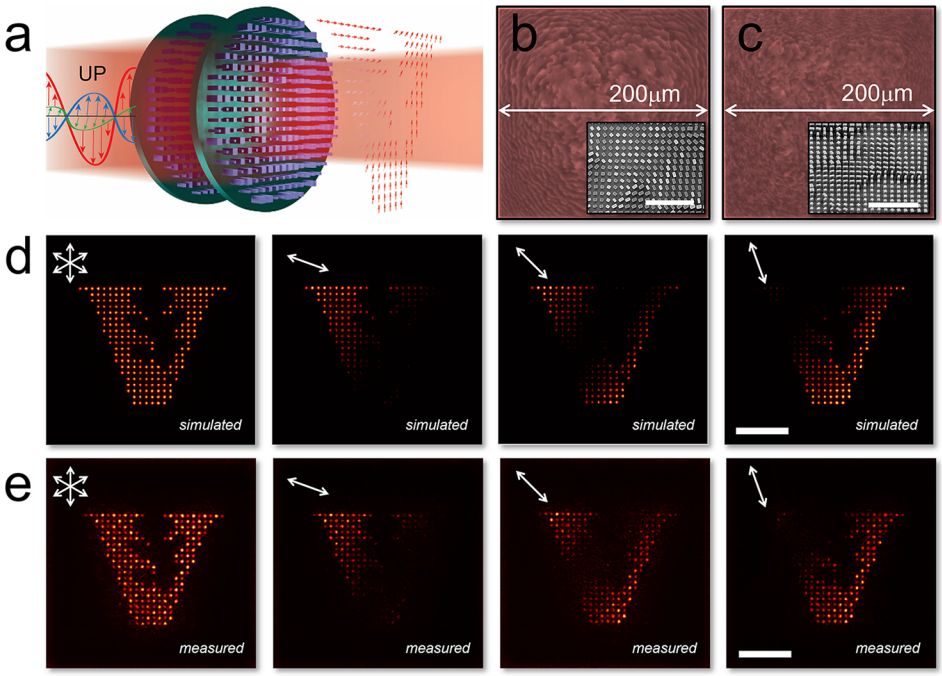

Figure 5. Meta-optic-based vectorial hologram. (a) Schematic of the multilayer meta-optic for the vectorial hologram to unpolarized beams. (b and c) Optical images of each metasurface in the meta-optic. The insets are SEM images of metasurfaces. Scale bar: 4 μm. (d and e) Simulated and measured polarization-dependent intensity distributions after the meta-optic. An unpolarized supercontinuum laser was used as the source. The upper-left corner arrows indicate the analyzer orientation. From the left to right, the analyzer state is unpolarized, 15°, 45°, and 75° polarized to the *x*-axis. Scale bar: 50 μm.

each polarization channel can be found in the Supporting Information (S3). Both metasurface layers exhibit a smooth profile, and the optical and scanning electron microscope (SEM) images are shown in Figure 3b,c, respectively. The meta-optic was characterized by imaging the far-field beam profiles for both polarizations with the results presented in Figure 3d,e. The measured beams exhibit a Gaussian profile with each beam being composed of the desired polarization component. The quantitative comparison of the beam intensity distribution between the simulated and measured results are presented in Figure 3f, showing excellent agreement and sub-1 μm experimental alignment accuracy (see detailed discussion in the Supporting Information (S5)). Furthermore, the diffraction efficiency, defined by the intensity in the two Gaussian beams over the input energy, with Fresnel reflection correction, was measured to be 88.64%. As a comparison, a single-layer metasurface with the same function has a maximum theoretical efficiency of only 5.3% (see other instances in the Supporting Information (S1)).

The design freedom associated with this approach can also be used to realize a meta-optic that acts as an arbitrary mode converter, allowing for the transfer of any polarization state across the Poincare sphere. As an example, we used the meta-optic to convert a single polarization state into two, while maintaining high conversion efficiency. Specifically, the desired output field at the second metasurface layer was given by,

$$\begin{bmatrix} E_x \\ E_y \end{bmatrix} = \begin{bmatrix} e^{-(r/28.3\lambda_0)^2} e^{ik_0 y\cdot\sin(0.03^\circ)} e^{i\pi/2} + e^{-(r/35\lambda_0)^2} e^{ik_0 y\cdot\sin(-0.03^\circ)} \\ e^{-(r/28.3\lambda_0)^2} e^{ik_0 y\cdot\sin(0.03^\circ)} + e^{-(r/35\lambda_0)^2} e^{ik_0 y\cdot\sin(-0.03^\circ)} e^{i\pi/2} \end{bmatrix} \tag{5}$$

Equation 5 divides the overall intensity into two Gaussian beams, with one being lefthand-circular-polarized (LCP) and the other righthand-circular-polarized (RCP), as shown in Figure 4a. The resulting phase profile can be found in the Supporting Information (S6), while the optical and SEM images are provided in Figure 4b,c, respectively. It is important to note that, even though we demonstrate conversion from a single state to two orthogonal states, multiple and arbitrary output states are also achievable using the end-to-end inverse-design process (see details in the Supporting Information (S7)), providing a powerful tool for enhancing the capacity of free-space optical communication systems.

The simulation and characterization of the far-field intensity distribution of the mode converter are shown in Figure 4d,e, with both output beams having a Gaussian-like shape. The polarization states, characterized by a quarter waveplate combined with a linear polarizer, demonstrate an excellent match with the theoretical predictions, with the exception of ripples observed at the edges due to diffraction from the neighboring aperture. The agreement between the simulated and measured results can also be found in the quantitative analysis of the intensity distribution shown in Figure 4f. The meta-optic has a measured diffraction efficiency, with Fresnel reflection correction, of 82.44%. The slight decrease in efficiency compared to the SDM meta-optic may be due to the inclusion of a varying rotation angle for each metasurface pixel, leading to additional fabrication errors.

The extra design degrees of freedom associated with multilayer meta-optics ultimately enable loss-less polarized complex-field control, which is not possible using a single-layer metasurface. To illustrate the full power of this approach, we demonstrate a meta-optic vectorial hologram,[50,51] in which polarization information is arbitrary redistributed on an image plane, as shown in Figure 5a. Specifically, we demonstrate a meta-optic that accepts unpolarized incident light and

https://doi.org/10.1021/acsnano.2c06248
ACS Nano 2022, 16, 15100−15107

redistributes the energy, based on polarization, to realize a "V" logo. The detailed phase profile, as well as rotation angle of the meta-atoms, can be found in the Supporting Information (S8). In Figure 5b,c, we present the optical and SEM images of the fabricated metasurfaces. The polarization distribution after the meta-optic was characterized using a linear analyzer, as shown in Figure 5d,e, demonstrating excellent agreement between the simulated and measured results. The diffraction efficiency, defined by the overall transmission over total input energy, was measured to be 83.0%.

The vectorial hologram devices manipulate the orthogonally polarized amplitude as well as polarization conversion efficiency, providing a powerful toolbox for optical systems design, which may find applications in a variety of areas. The cascaded architecture and the ability to redistribute light across the aperture enable opportunities in optical computing, such as neural networks,[52] where low-loss spatial control over the output field is necessary. Meanwhile, complete control over the coherent vector field along orthogonal axes can be used for quantum entanglement[53] with spin and orbital angular momentum encoded in the optic. Furthermore, high-efficiency and arbitrary spatial mode manipulation allow for optical multiplexing and division for use in multichannel displays[27] and information encryption.[54,55]

CONCLUSION

In summary, we have demonstrated a meta-optic platform that combines birefringence with the ability to redistribute the wavefront across the aperture, leading to near loss-less control over the amplitude, phase, and polarization state. The use of a second metasurface provides additional design flexibility, allowing one to overcome the limitations arising from the symmetric Jones matrix that dictates the capabilities of single-layer metasurfaces. Combined with end-to-end optimization, this platform can be used for a wide variety of purposes including SDM, mode conversion, and complex vectorial holograms with efficiencies over 80.0% being demonstrated here. Moreover, this platform can be readily extended to many-layer systems with multidimensional parameters allowing for optical computing, quantum entanglement, optical encryption, and optical communications applications.

METHODS

Numerical Simulation. The complex transmissive coefficient of the silicon nanopillar meta-atoms was obtained using an open-source rigorous coupled analysis (RCWA) solver, Reticolo.[56] A square lattice with a period of 0.52 μm was used with a design wavelength of 1.15 μm. The height of the silicon nanopillars was fixed at 0.75 μm. The index was set at 3.79 based on ellipsometry of the α-Si films. The meta-atom was embedded within a material with an index of 1.48 to simulate a PMMA encapsulation layer.

Stochastic Gradient Descent-Based Inverse Design. The inverse design of the compound meta-optics was achieved using end-to-end optimization within Pytorch (1.10.2) and the CUDA toolkit (11.3.1) for GPU accelerated stochastic gradient descent (SGD). For each meta-atom in the metasurface layer, the phase shift along orthogonal directions, ϕ_x and ϕ_y, and the geometrical rotation angle, θ, was used as the optimization parameters. The complex-valued electric field, propagated away from the meta-optic to various distances, served as the optimization target. Since the field contained complex amplitude values, the mean square error (MSE) served as the error function. The backpropagation was achieved by the ADAM solver with 1000 epochs performed in total during optimization.

Metasurface Fabrication. EBL-based lithography was used to fabricate the metasurfaces. Low-pressure chemical vapor deposition (LPCVD) was first used to deposit a 0.75 μm thick silicon device layer on a quartz substrate. PMMA-950 K-A4 photoresist was spin-coated on the silicon layer followed by evaporation of a 10 nm thick Cr conduction layer. EBL patterning was then performed and after removing the Cr layer, the exposed pattern was developed with MIBK. A 50 nm Al_2O_3 hard mask was deposited *via* electron beam evaporation, followed by lift-off. The silicon was then patterned using reactive ion etching, and a 1 μm thick layer of PMMA was spin-coated to encase the nanopillar structures as a protective and index-matching layer.

Optical Characterization. In order to fabricate and characterize the compound meta-optics, an in situ alignment system was utilized (see the Supporting Information (S4)). The bilayer metasurface alignment process was achieved by an XYZ translation and a rotation stage. First, the bottom layer was fixed on a rotational stage by a vacuum pump, while the top layer was carried by the translation stage. Then, a drop of uncured PDMS was applied in between as an index-matched layer. The samples were then illuminated from the bottom by a collimated laser at the designed working wavelength. Alignment of the layers was accomplished by overlapping an alignment hologram and the top layer metasurface with a registration pattern. Far-field images, after the bilayer metasurface, were recorded by a NIR camera through an imaging system consisting of a 50× objective and a tube lens. The efficiency was calculated based on the images captured by the NIR camera. The reference intensity was calculated from images of the substrates without any meta-optics. The efficiency of the SDM and mode converter devices was calculated based on the intensity within an area encompassing each beam in the far field, divided by the reference intensity. For the vectorial hologram, the efficiency is the intensity contained in the transmitted field divided by the reference intensity.

ASSOCIATED CONTENT

Supporting Information

The Supporting Information is available free of charge at https://pubs.acs.org/doi/10.1021/acsnano.2c06248.

> Comparison of the complex-amplitude modulation methods, target fields for spatial mode division multiplexing, spatial mode converter, and universal vectorial hologram, comparison of compound meta-optic phase profiles, bilayer metasurfaces alignment system and alignment marks, simulated sensitivity to lateral misalignment and vertical misalignment, phase profiles for the meta-optic spatial mode converter and multi-channel mode converter, comparison of the target and simulated intensity profiles of the multi-channel mode converter, and phase profile of the universal vectorial hologram and discussions of details of inverse design parameters (PDF)

AUTHOR INFORMATION

Corresponding Author

Jason G. Valentine − *Department of Mechanical Engineering, Vanderbilt University, Nashville, Tennessee 37212, United States;* orcid.org/0000-0001-9943-7170; Email: jason.g.valentine@vanderbilt.edu

Authors

Hanyu Zheng − *Department of Electrical and Computer Engineering, Vanderbilt University, Nashville, Tennessee 37212, United States*

Mingze He − *Department of Mechanical Engineering, Vanderbilt University, Nashville, Tennessee 37212, United States;* orcid.org/0000-0001-8773-1268

https://doi.org/10.1021/acsnano.2c06248
ACS Nano 2022, 16, 15100−15107

You Zhou − *Interdisciplinary Materials Science Program, Vanderbilt University, Nashville, Tennessee 37212, United States;* orcid.org/0000-0002-5810-2347

Ivan I. Kravchenko − *Center for Nanophase Materials Sciences, Oak Ridge National Laboratory, Oak Ridge, Tennessee 37830, United States*

Joshua D. Caldwell − *Department of Mechanical Engineering, Vanderbilt University, Nashville, Tennessee 37212, United States;* orcid.org/0000-0003-0374-2168

Complete contact information is available at: https://pubs.acs.org/10.1021/acsnano.2c06248

Author Contributions

H.Z. and J.G.V developed the idea. H.Z. and Y.Z. conducted the optical modeling and system design. M.H and H.Z. developed the inverse design platform. H.Z fabricated the samples. I.I.K. performed the silicon growth. H.Z. performed the experimental measurements and data analysis. H.Z. and J.G.V. wrote the manuscript with input from all the authors. The project was supervised by J.G.V. and J.D.C.

Notes

The authors declare no competing financial interest.

ACKNOWLEDGMENTS

H.Z., Y.Z., and J.G.V. acknowledge financial support from the Office of Naval Research under grant number N00014-18-1-2568. M.H. and J.D.C. both acknowledge financial support from the Office of Naval Research under grant number N00014-22-1-2035. Part of the fabrication process was conducted at the Center for Nanophase Materials Sciences, which is a DOE Office of Science User Facility. The remainder of the fabrication process took place in the Vanderbilt Institute of Nanoscale Science and Engineering (VINSE), and the authors thank the staff for their support.

REFERENCES

(1) Yu, N.; Capasso, F. Flat Optics with Designer Metasurfaces. *Nat. Mater.* **2014**, *13* (2), 139−150.

(2) Kamali, S. M.; Arbabi, E.; Arbabi, A.; Faraon, A. A Review of Dielectric Optical Metasurfaces for Wavefront Control. *Nanophotonics* **2018**, *7* (6), 1041−1068.

(3) Zhang, Y. B.; Liu, H.; Cheng, H.; Tian, J. G.; Chen, S. Q. Multidimensional Manipulation of Wave Fields Based on Artificial Microstructures. *Opto-Electronic Adv.* **2020**, *3* (11), 200002.

(4) Dorrah, A. H.; Capasso, F. Tunable Structured Light with Flat Optics. *Science* **2022**, *376* (6591), 1.

(5) Arbabi, A.; Horie, Y.; Ball, A. J.; Bagheri, M.; Faraon, A. Subwavelength-Thick Lenses with High Numerical Apertures and Large Efficiency Based on High-Contrast Transmitarrays. *Nat. Commun.* **2015**, *6* (1), 2−7.

(6) Khorasaninejad, M.; Chen, W. T.; Devlin, R. C.; Oh, J.; Zhu, A. Y.; Capasso, F. Metalenses at Visible Wavelengths: Diffraction-Limited Focusing and Subwavelength Resolution Imaging. *Science (80-.).* **2016**, *352* (6290), 1190−1194.

(7) Zhang, L.; Ding, J.; Zheng, H.; An, S.; Lin, H.; Zheng, B.; Du, Q.; Yin, G.; Michon, J.; Zhang, Y.; Fang, Z.; Shalaginov, M. Y.; Deng, L.; Gu, T.; Zhang, H.; Hu, J. Ultra-Thin High-Efficiency Mid-Infrared Transmissive Huygens Meta-Optics. *Nat. Commun.* **2018**, *9* (1), 1481.

(8) Ding, F.; Deshpande, R.; Meng, C.; Bozhevolnyi, S. I. Metasurface-Enabled Broadband Beam Splitters Integrated with Quarter-Wave Plate Functionality. *Nanoscale* **2020**, *12* (26), 14106−14111.

(9) Zhu, L.; Liu, X.; Sain, B.; Wang, M.; Schlickriede, C.; Tang, Y.; Deng, J.; Li, K.; Yang, J.; Holynski, M.; Zhang, S.; Zentgraf, T.; Bongs, K.; Lien, Y. H.; Li, G. A Dielectric Metasurface Optical Chip for the Generation of Cold Atoms. *Sci. Adv.* **2020**, *6* (31), 4−9.

(10) Yang, Y.; Yoon, G.; Park, S.; Namgung, S. D.; Badloe, T.; Nam, K. T.; Rho, J. Revealing Structural Disorder in Hydrogenated Amorphous Silicon for a Low-Loss Photonic Platform at Visible Frequencies. *Adv. Mater.* **2021**, *33* (9), 2005893.

(11) Tao, J.; You, Q.; Li, Z.; Luo, M.; Liu, Z.; Qiu, Y.; Yang, Y.; Zeng, Y.; He, Z.; Xiao, X.; Zheng, G.; Yu, S. Mass-Manufactured Beam-Steering Metasurfaces for High-Speed Full-Duplex Optical Wireless-Broadcasting Communications. *Adv. Mater.* **2022**, *34* (6), 2106080.

(12) Shi, Z.; Zhu, A. Y.; Li, Z.; Huang, Y.-W.; Chen, W. T.; Qiu, C.-W.; Capasso, F. Continuous Angle-Tunable Birefringence with Freeform Metasurfaces for Arbitrary Polarization Conversion. *Sci. Adv.* **2020**, *6* (23), 1−8.

(13) Deng, Y.; Wu, C.; Meng, C.; Bozhevolnyi, S. I.; Ding, F. Functional Metasurface Quarter-Wave Plates for Simultaneous Polarization Conversion and Beam Steering. *ACS Nano* **2021**, *15* (11), 18532−18540.

(14) Zhou, Y.; Kravchenko, I. I.; Wang, H.; Nolen, J. R.; Gu, G.; Valentine, J. Multilayer Noninteracting Dielectric Metasurfaces for Multiwavelength Metaoptics. *Nano Lett.* **2018**, *18* (12), 7529−7537.

(15) Rubin, N. A.; D'Aversa, G.; Chevalier, P.; Shi, Z.; Chen, W. T.; Capasso, F. Matrix Fourier Optics Enables a Compact Full-Stokes Polarization Camera. *Science* **2019**, *364* (6448), 1.

(16) Kim, J.; Seong, J.; Yang, Y.; Moon, S. W.; Badloe, T.; Rho, J. Tunable Metasurfaces towards Versatile Metalenses and Metaholograms: A Review. *Adv. Photonics* **2022**, *4* (2), 1−16.

(17) Kwon, H.; Arbabi, E.; Kamali, S. M.; Faraji-Dana, M. S.; Faraon, A. Single-Shot Quantitative Phase Gradient Microscopy Using a System of Multifunctional Metasurfaces. *Nat. Photonics* **2020**, *14* (2), 109−114.

(18) Zhou, Y.; Zheng, H.; Kravchenko, I. I.; Valentine, J. Flat Optics for Image Differentiation. *Nat. Photonics* **2020**, *14* (5), 316−323.

(19) Huo, P.; Zhang, C.; Zhu, W.; Liu, M.; Zhang, S.; Zhang, S.; Chen, L.; Lezec, H. J.; Agrawal, A.; Lu, Y.; Xu, T. Photonic Spin-Multiplexing Metasurface for Switchable Spiral Phase Contrast Imaging. *Nano Lett.* **2020**, *20* (4), 2791−2798.

(20) Lan, S.; Zhang, X.; Taghinejad, M.; Rodrigues, S.; Lee, K. T.; Liu, Z.; Cai, W. Metasurfaces for Near-Eye Augmented Reality. *ACS Photonics* **2019**, *6* (4), 864−870.

(21) Lee, G. Y.; Hong, J. Y.; Hwang, S. H.; Moon, S.; Kang, H.; Jeon, S.; Kim, H.; Jeong, J. H.; Lee, B. Metasurface Eyepiece for Augmented Reality. *Nat. Commun.* **2018**, *9* (1), 1−10.

(22) Lee, G. Y.; Yoon, G.; Lee, S. Y.; Yun, H.; Cho, J.; Lee, K.; Kim, H.; Rho, J.; Lee, B. Complete Amplitude and Phase Control of Light Using Broadband Holographic Metasurfaces. *Nanoscale* **2018**, *10* (9), 4237−4245.

(23) Gao, H.; Fan, X.; Xiong, W.; Hong, M. Recent Advances in Optical Dynamic Meta-Holography. *Opto-Electronic Adv.* **2021**, *4* (11), 210030.

(24) Kim, J.; Yang, Y.; Badloe, T.; Kim, I.; Yoon, G.; Rho, J. Geometric and Physical Configurations of Meta-Atoms for Advanced Metasurface Holography. *InfoMat* **2021**, *3* (7), 739−754.

(25) Kim, J.; Oh, D. K.; Kim, H.; Yoon, G.; Jung, C.; Kim, J.; Badloe, T.; Kang, H.; Kim, S.; Yang, Y.; Lee, J.; Ko, B.; Ok, J. G.; Rho, J. Metasurface Holography Reaching the Highest Efficiency Limit in the Visible via One-Step Nanoparticle-Embedded-Resin Printing. *Laser Photonics Rev.* **2022**, *16* (8), 2200098.

(26) Zaidi, A.; Rubin, N. A.; Dorrah, A.; Shi, Z.; Capasso, F. Jones Matrix Holography with Metasurfaces. *Sci. Adv.* **2021**, *7* (33), 1−9.

(27) Zhao, R.; Sain, B.; Wei, Q.; Tang, C.; Li, X.; Weiss, T.; Huang, L.; Wang, Y.; Zentgraf, T. Multichannel Vectorial Holographic Display and Encryption. *Light Sci. Appl.* **2018**, *7* (1), 95.

(28) Deng, Z. L.; Deng, J.; Zhuang, X.; Wang, S.; Li, K.; Wang, Y.; Chi, Y.; Ye, X.; Xu, J.; Wang, G. P.; Zhao, R.; Wang, X.; Cao, Y.; Cheng, X.; Li, G.; Li, X. Diatomic Metasurface for Vectorial Holography. *Nano Lett.* **2018**, *18* (5), 2885−2892.

(29) Divitt, S.; Zhu, W.; Zhang, C.; Lezec, H. J.; Agrawal, A. Ultrafast Optical Pulse Shaping Using Dielectric Metasurfaces. *Science.* **2019**, *364* (6443), 890−894.
(30) Overvig, A. C.; Shrestha, S.; Malek, S. C.; Lu, M.; Stein, A.; Zheng, C.; Yu, N. Dielectric Metasurfaces for Complete and Independent Control of the Optical Amplitude and Phase. *Light Sci. Appl.* **2019**, *8* (1), 92.
(31) Deng, Z. L.; Jin, M.; Ye, X.; Wang, S.; Shi, T.; Deng, J.; Mao, N.; Cao, Y.; Guan, B. O.; Alù, A.; Li, G.; Li, X. Full-Color Complex-Amplitude Vectorial Holograms Based on Multi-Freedom Metasurfaces. *Adv. Funct. Mater.* **2020**, *30* (21), 1910610.
(32) Lung, S.; Wang, K.; Kamali, K. Z.; Zhang, J.; Rahmani, M.; Neshev, D. N.; Sukhorukov, A. A. Complex-Birefringent Dielectric Metasurfaces for Arbitrary Polarization-Pair Transformations. *ACS Photonics* **2020**, *7* (11), 3015−3022.
(33) Wang, Q.; Zhang, X.; Xu, Y.; Gu, J.; Li, Y.; Tian, Z.; Singh, R.; Zhang, S.; Han, J.; Zhang, W. Broadband Metasurface Holograms: Toward Complete Phase and Amplitude Engineering. *Sci. Rep.* **2016**, *6*, 32867.
(34) Zhou, Y.; Kravchenko, I. I.; Wang, H.; Zheng, H.; Gu, G.; Valentine, J. Multifunctional Metaoptics Based on Bilayer Metasurfaces. *Light Sci. Appl.* **2019**, *8* (1), 80.
(35) Tanaka, K.; Arslan, D.; Fasold, S.; Steinert, M.; Sautter, J.; Falkner, M.; Pertsch, T.; Decker, M.; Staude, I. Chiral Bilayer All-Dielectric Metasurfaces. *ACS Nano* **2020**, *14* (11), 15926−15935.
(36) Li, Z.; Liu, W.; Cheng, H.; Choi, D. Y.; Chen, S.; Tian, J. Arbitrary Manipulation of Light Intensity by Bilayer Aluminum Metasurfaces. *Adv. Opt. Mater.* **2019**, *7* (13), 1900260.
(37) Raeker, B. O.; Grbic, A. Compound Metaoptics for Amplitude and Phase Control of Wave Fronts. *Phys. Rev. Lett.* **2019**, *122* (11), 113901.
(38) Raeker, B. O.; Zheng, H.; Zhou, Y.; Kravchenko, I. I.; Valentine, J.; Grbic, A. All-Dielectric Meta-Optics for High-Efficiency Independent Amplitude and Phase Manipulation. *Adv. Photonics Res.* **2022**, *3* (3), 2100285.
(39) Mansouree, M.; Kwon, H.; Arbabi, E.; McClung, A.; Faraon, A.; Arbabi, A. Multifunctional 25D Metastructures Enabled by Adjoint Optimization. *Optica* **2020**, *7* (1), 77.
(40) Wang, Z. X.; Wu, J. W.; Wu, L. W.; Gou, Y.; Ma, H. F.; Cheng, Q.; Cui, T. J. High Efficiency Polarization-Encoded Holograms with Ultrathin Bilayer Spin-Decoupled Information Metasurfaces. *Adv. Opt. Mater.* **2021**, *9* (5), 2001609.
(41) Deng, L.; Li, Z.; Zhou, Z.; He, Z.; Zeng, Y.; Zheng, G.; Yu, S. Bilayer-Metasurface Design, Fabrication, and Functionalization for Full-Space Light Manipulation. *Adv. Opt. Mater.* **2022**, *10* (7), 2102179.
(42) Mirzapourbeinekalaye, B.; McClung, A.; Arbabi, A. General Lossless Polarization and Phase Transformation Using Bilayer Metasurfaces. *Adv. Opt. Mater.* **2022**, *10* (11), 2102591.
(43) Kruk, S.; Ferreira, F.; Mac Suibhne, N.; Tsekrekos, C.; Kravchenko, I.; Ellis, A.; Neshev, D.; Turitsyn, S.; Kivshar, Y. Transparent Dielectric Metasurfaces for Spatial Mode Multiplexing. *Laser Photonics Rev.* **2018**, *12* (8), 1800031.
(44) Nazemosadat, E.; Mazur, M.; Kruk, S.; Kravchenko, I.; Carpenter, J.; Schröder, J.; Andrekson, P. A.; Karlsson, M.; Kivshar, Y. Dielectric Broadband Metasurfaces for Fiber Mode-Multiplexed Communications. *Adv. Opt. Mater.* **2019**, *7* (14), 1801679.
(45) Xie, Y.-Y.; Ni, P.-N.; Wang, Q.-H.; Kan, Q.; Briere, G.; Chen, P.-P.; Zhao, Z.-Z.; Delga, A.; Ren, H.-R.; Chen, H.-D.; Xu, C.; Genevet, P. Metasurface-Integrated Vertical Cavity Surface-Emitting Lasers for Programmable Directional Lasing Emissions. *Nat. Nanotechnol.* **2020**, *15* (2), 125.
(46) Liu, W.; Yang, Q.; Xu, Q.; Jiang, X.; Wu, T.; Wang, K.; Gu, J.; Han, J.; Zhang, W. Multifunctional All-Dielectric Metasurfaces for Terahertz Multiplexing. *Adv. Opt. Mater.* **2021**, *9* (19), 2100506.
(47) Kingma, D. P.; Ba, J. L. Adam: A Method for Stochastic Optimization. *3rd International Conference for Learning Representations*, San Diego, CA, May 7−9, 2015.
(48) Kulce, O.; Mengu, D.; Rivenson, Y.; Ozcan, A. All-Optical Synthesis of an Arbitrary Linear Transformation Using Diffractive Surfaces. *Light Sci. Appl.* **2021**, *10* (1), 25.
(49) Raeker, B. O.; Grbic, A. Lossless Complex-Valued Optical-Field Control with Compound Metaoptics. *Phys. Rev. Appl.* **2021**, *15* (5), 1−13.
(50) Arbabi, E.; Kamali, S. M.; Arbabi, A.; Faraon, A. Vectorial Holograms with a Dielectric Metasurface: Ultimate Polarization Pattern Generation. *ACS Photonics* **2019**, *6* (11), 2712−2718.
(51) Wen, D.; Cadusch, J. J.; Meng, J.; Crozier, K. B. Vectorial Holograms with Spatially Continuous Polarization Distributions. *Nano Lett.* **2021**, *21* (4), 1735−1741.
(52) Zheng, H.; Liu, Q.; Zhou, Y.; Kravchenko, I. I.; Huo, Y.; Valentine, J. Meta-Optic Accelerators for Object Classifiers. *Sci. Adv.* **2022**, *8* (30), eabo6410.
(53) Stav, T.; Faerman, A.; Maguid, E.; Oren, D.; Kleiner, V.; Hasman, E.; Segev, M. Quantum Entanglement of the Spin and Orbital Angular Momentum of Photons Using Metamaterials. *Science (80-.).* **2018**, *361* (6407), 1101−1104.
(54) Georgi, P.; Qunshuo, W.; Sain, B.; Schlickriede, C.; Wang, Y.; Huang, L.; Zentgraf, T. Cascaded Metasurface Holograms for Optical Secret Sharing. *CLEO: QELS_Fundamental Science 2021*, San Jose, CA, May 9−14, 2021.
(55) Kim, I.; Jang, J.; Kim, G.; Lee, J.; Badloe, T.; Mun, J.; Rho, J. Pixelated bifunctional metasurface-driven dynamic vectorial holographic color prints for photonic security platform. *Nat. Commun.* **2021**, *12* (1), 3614.
(56) Hugonin, A. J. P.; Lalanne, P. RETICOLO CODE 1D for the Diffraction by Stacks of Lamellar 1D Gratings. *ArXiv* **2012**, 1−16.

https://doi.org/10.1021/acsnano.2c06248
ACS Nano 2022, 16, 15100−15107